Available online at www.sciencedirect.com
SCIENCE DIRECT®
Journal of volcanology and geothermal research
ELSEVIER
Journal of Volcanology and Geothermal Research 129 (2004) 173–197
www.elsevier.com/locate/jvolgeores

Analog experiments on melting and contamination at the roof and walls of magma chambers

A.M. Leitch *

Department of Earth Sciences, Memorial University, St John's, NF, Canada A1B 3X5

Received in revised form 22 March 2002; accepted 22 April 2003

Abstract

A series of analogue laboratory experiments were carried out to model melting and mixing processes occurring at the roof and sides of a magma chamber when hot, dense mantle-derived magmas are emplaced in the deep crust. The experiments investigated the influence of a viscosity contrast between crustal melts and input magma, the presence of crystals in the input magma, and roof geometry. The crust was modelled by aqueous ice or a cold, low-melting point wax, arranged as a flat roof or in an upside-down U. The input magma was modelled by a hot, dense aqueous solution of $NaNO_3$ or $FeSO_4$, which was injected into the cavity between the walls. The experiments revealed the potentially important role that side-wall processes may have in crustal melting and mantle magma contamination in this environment. The walls melted back much faster than the roof and the melts from the opposite walls ponded next to each other under the roof and mixed with each other only in the central region. When the input solution was able to crystallise, it did so preferentially in the active side-wall boundary layers. The tiny, dense crystals, which were dragged up in the melt boundary layer and then dropped into the interior fluid, enhanced hybridisation of the melt and contamination of the input fluid and, through their influence on the boundary layer structure, reduced the melting rate.

Keywords: magma chambers; analogue experiments; melting; magma mixing

1. Introduction

The diversity of igneous rocks in the Earth's continental crust arises from a diverse range of processes, such as fractional crystallisation of mantle melts, partial to complete melting of existing crustal rocks, magma mixing and hybridisation, assimilation of country rock, and liquid immiscibility. The heat required for crustal melting may arise from radiogenic heating of thickened crust or heat conducted from the mantle through thinned asthenosphere (Thompson and Connolly, 1995), but the major source is likely to be underplating or intrusion of the crust by mantle-derived mafic magmas (Huppert and Sparks, 1988; Bergantz, 1989), because the proximity of hot magmas to fuseable crust allows for efficient heat exchange. Underplating is inferred in many tectonic scenarios: in back arcs (Yanagi and Maeda, 1998), continental margins (Saleeby et al., 2003),

* Tel.: +1-709-737-3306; Fax: +1-709-737-2589.
E-mail address: aleitch@mun.ca (A.M. Leitch).

0377-0273/03/$ – see front matter © 2003 Elsevier B.V. All rights reserved.
doi:10.1016/S0377-0273(03)00239-7

flood basalt provinces (Farnetani et al., 1996; Wilson and Wheeler, 2002) and hot spots (CD-ROM Working Group, 2002). In convergent margins the generation of silicic rocks during underplating is likely to be a multistage process, involving fractionation of hydrous mafic magmas and remelting of hydrous cumulates by subsequent intrusions (Saleeby et al., 2003; Weinberg and Dunlop, 2000), though geochemical signatures sometimes indicate that the original crust is also involved in the melting (Saleeby et al., 2003). Further processes are involved in the transport and emplacement of magmas (Brown, 1994; Petford et al., 2000), which may be by dykes, pervasive flow through a network of channels (Brown, 1994; Weinberg, 1999) or diapirs (Weinberg and Podladchikov, 1994), depending on the tectonics and thermal structure of the crust (e.g. Leitch and Weinberg, 2002).

Although heat from intruded mantle magmas is likely involved in crustal melting, the dynamics of the processes is uncertain. From a purely thermal point of view, melting would occur most efficiently directly at the contact between a mantle magma and crust, when the latent heat of crystallisation of the mantle magma could be used to melt a similar volume of crust (Bowen, 1928). Assimilation–fractional crystallisation (AFC) processes, where the heat of crystallisation is used to melt adjacent and incorporated crustal material, were put forward to explain mixed crustal and mantle signatures of continental margin rocks (DePaolo, 1981; DePaolo and Farmer, 1984). However, cross-contamination of crustal melts and mantle magmas is perceived to be inhibited by the different physical properties of the magmas (Frost and Mahood, 1987) and the geometry of the contacts. Campbell and Turner (1987) argued that fractional crystallisation and crustal melting in large layered intrusions would be separated by one or more double-diffusive interfaces at the top of the magma chamber, and that limited contamination on the mafic magma would occur due to stoping or melting at a side wall. Melting at bottom contacts, which would at least initially promote contamination (Kaneko and Koyaguchi, 2000), would be inhibited by the settling and growth of crystals on the contact (Kerr, 1994). In some circumstances, influx of felsic magma into an overlying mafic chamber may overcome these inhibiting factors (Weinberg and Leitch, 1998).

The purpose of the present work is to extend experimental investigations on dynamical processes at the roof and walls of a magma chamber. This work follows on from that of Campbell and Turner (1987), Huppert and Sparks (1988) and Kerr (1994). Campbell and Turner (1987) modelled AFC processes by emplacing a hot, saturated aqueous fluid (analogue to a mafic magma) beneath a mixed ice (analogue to the crust). Huppert and Sparks (1988) modelled crustal melting at a horizontal roof during underplating using unsaturated aqueous solutions as analogue magma and wax, which produces a high-viscosity melt, as analogue crust. Kerr (1994) analysed the melting of a sloping wax roof. The experiments described here are a systematic investigation of the effects of the geometry (sloping and horizontal roof) of the melt-input contact, the viscosity contrast of melt and input fluid (using ice and wax as crustal analogues), and crystallisation of the input fluid on the rates of melting, and processes of mixing and contamination at the contact. Neither Huppert and Sparks (1988) nor Kerr (1994) included crystallisation of the analogue basaltic magma in their experimental investigations, though they discussed possible ramifications. Campbell and Turner (1987) used aqueous solutions of Na_2CO_3 as an analogue magma, and this chemical tended to crystallise in situ on the floor of the chamber, so that, though latent heat was released and the composition of the input fluid evolved, the melt-input contact was crystal-free. For this investigation, the crystallising input fluids were concentrated aqueous solutions of $FeSO_4$ and $NaNO_3$, and these nucleated tiny, dense crystals (like a slurry of individual olivine or pyroxene crystals) very close to the contact, where they could and did affect heat and mass transfer.

In the sections below, the experimental setup and results for the three different contact geometries are given. The appendices contain mathematical analyses of the side-wall boundary layers, which were central to the evolution of the experi-

ments. Side-wall boundary layers led to efficient melting of the walls and simultaneously inhibited melting of the roof. Low-viscosity melts produced thinner boundary layers, which allowed chemical diffusion to modify the melt composition. Crystals nucleating in the boundary layer affected melting and contamination differently depending on geometry and viscosity contrasts, but almost always led to a decrease in the melting rate.

2. Experimental setup and procedure

Nomenclature is given in Table 1. The experiments were carried out in a rectangular tank with front and back walls of perspex, and a roof, floor and two walls which can be heat exchangers or perspex (Fig. 1). The bottom of the tank was filled with a tight-fitting insulator, so the experimental region was 8 cm high, 30 cm wide and 15 cm deep. The top and one or two sides of this region were filled with a solid representing the crust, leaving a cavity 5 cm deep. Alcohol was pumped through the heat exchanger walls, maintaining them at a few degrees below the melting temperature of the solid. Keeping the boundary temperature close to the melting temperature minimised the influence of the proximity of the heat exchangers.

Table 1
Nomenclature

Symbol	Definition	Units
A	surface area	m^2
c	specific heat at constant pressure	J/kg/°C
C	(salt) concentration	wt%
D	chemical diffusivity	m^2/s
f	crystallisation fraction	1
g	acceleration of gravity	m/s^2
h	boundary layer thickness	m, cm, mm
H	vertical height	cm, m
k	thermal conductivity	W/m/°C
L	latent heat	J/kg
q	heat flux	W/m^2
Q	volume flux	m^3/s
t	time	min, s
T	temperature	°C
ΔT	superheat/supercooling	°C
U	fluid velocity	m/s
v	melt rate	m/s
V	volume	m^3
x	horizontal distance	cm, m
X	horizontal melt-back of walls	cm, m
z	vertical distance	m
Z	vertical melt-back of roof	cm, m
α	thermal expansivity	$°C^{-1}$
β	compositional expansivity	$wt\%^{-1}$
κ	thermal diffusivity	m^2/s
μ	dynamic viscosity	kg/m/s
ρ	density	kg/m^3
Subscripts		
0	initial value	
m	melt	
D	chemical diffusion	
f	input fluid	
s	solid	
sat	saturation condition	
T	thermal	

To prepare the solid, a dummy block was placed in the position of the cavity and the tank on either side filled with (separately dyed) melts. These were frozen from the heat exchanger walls, and then the roof solution was emplaced and frozen from above. The dummy block was then removed.

At the start of an experiment the cavity was filled, from a 1-cm diameter plastic pipe through the roof or one side, with hot aqueous solution. Another pipe through the centre of the roof allowed the escape of air and the insertion of temperature probes and sampling tubes. The position of the probes was adjusted by hand to take vertical profiles. Temperatures recorded by the probes within the tank and the heat exchanger walls were digitally logged, and the density of fluid samples was measured by a densimeter. The tank was back-lit by a projector and front-lit by room lighting. Slide photographs were taken at regular intervals and from these the melting rate of the walls and roof were measured.

2.1. Geometry

The experiments were run in three geometries (Table 4). The 2WR experiments were set up as drawn in Fig. 1. Two walls sloped inward at 60° toward a flat roof, and each wall and the roof contained dyes of different colours. The initial aspect ratio A_0 (width:height) of the cavity was 2.5. For the WR experiments, the right-hand cavity wall was a vertical insulating boundary and

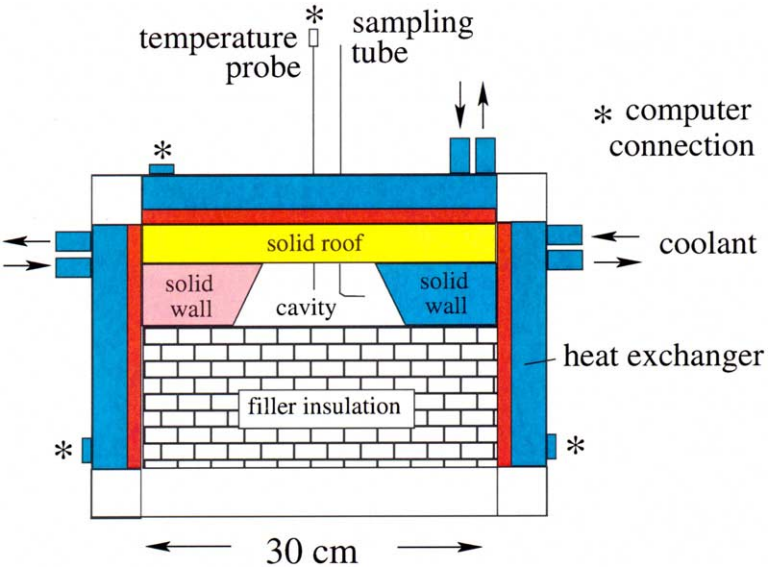

Fig. 1. Diagram of tank used to run the experiments, with model crust (dyed blocks in upper part of tank) set up in the geometry used for 2WR experiments.

$A_0 \approx 4$. The R experiments had two insulating walls, so the contact was at the horizontal roof only.

2.2. Analogue materials

Three analogues ('solids') were used to represent the crust: a polyethylene glycol wax (PEG-600), a eutectic ice of sodium carbonate and water (Na_2CO_3–H_2O) and a quasi-eutectic ice of ferrous sulphate and water ($FeSO_4$–H_2O). Physical properties of these solids and their melts are given in Table 2a,b. The experiments were named (Table 4) according to the geometry, solid composition (P, F or N) and a number, which indicates the order in which the experiments were carried out.

The use of eutectic ices rather than water ice simplified the dynamics (e.g. there was no density minimum as there is at 4°C for pure water) and allowed dye to be incorporated into the solids as they froze, so that melts could be tracked by their colours. Sodium carbonate eutectic ice formed a uniformly dyed homogeneous solid, but ferrous sulphate solutions supercooled several degrees under laboratory conditions and the solid was of uneven composition (see Section 4.3). These ices, like water ice, have a relatively large latent heat and significantly different thermal properties (k, c, κ) than their melts. PEG-600 wax is more like a

Table 2a
Properties of experimental and geological solids

Material	ρ_s (kg/m^3)	c_s (J/kg/°C)	k_s (W/m/°C)	κ_s (m^2/s)	T_m (°C)	L (J/kg)
Na_2CO_3–H_2O eutectic ice	968	1900	1.9	1.0×10^{-6}	−2.1	3.3×10^5
$FeSO_4$–H_2O eutectic ice	1033	1900[a]	1.9[a]	1.0×10^{-5}	−1.8	3.3×10^5[a]
PEG-600 wax	1210	2490	0.24	8×10^{-8}	19	1.46×10^5
Continental crust[b]	2700	1340	2.9	8×10^{-7}	850	2.9×10^5

[a] Guesses based on properties of Na_2CO_3–H_2O eutecticice.
[b] Huppert and Sparks, 1988.

Table 2b
Properties of experimental and geological fluids

Material	$T_{m,f}$ (°C)	$\rho_{m,f}$ (kg/m^3)	$c_{m,f}$ (J/kg/°C)	km,f (W/m/°C)	$\mu_{m,f}\times10^3$ (kg/m/s)	αm,f$\times10^4$ (°C^{-1})	$D_{m,f}$[a]$\times10^{10}$ (m^2/s)
Melt							
Na_2CO_3–H_2O	−2.1	1066	3900	0.55	2.6	2.1	5
$FeSO_4$–H_2O	−1.8	1140	3725[b]	0.54	2.0	2.5	5
PEG-600	19	1128	2660	0.24	180	7.6	
Continental crust[c]	850	2300	1340	2.9	10^9	0.5	≤0.1[d]
Input fluid							
25–20 wt% $FeSO_4$	35→8	1268→1220	3375→3515	0.58→0.54	0.8→1.6	5.4→4.1	
63–34 wt% $NaNO_3$	100→11	1515→1270	2673→3056	0.62→0.52	0.6→3.5	6.2→5.1	8
Basalt magma[c]	1200–1091	2700	1340	2.9	300 000	0.5	≤0.1

[a] Washburn, 1926.
[b] Guesses based on properties of Na_2CO_3–H_2O eutectic ice.
[c] Huppert and Sparks, 1988.
[d] Hofmann, 1980.

silicate in that the solid and melt have similar thermal properties. The wax is arguably also a better analogue crust in that the melt is much more viscous than the analogue magmas.

Two analogue magmas ('input fluids') were used: concentrated ferrous sulphate ($FeSO_4$) aqueous solutions, which were used only with ferrous sulphate ice, and sodium nitrate ($NaNO_3$) solutions, which were used with sodium carbonate ice and PEG wax. The input fluids were all hotter than the melting point of the solid and denser than the melts. Some fluids never formed crystals. Others (marked with * in Table 4) were saturated and so crystallised immediately upon input. Under laboratory conditions, the first-formed crystals were so small that their individual sizes could not be determined with the naked eye.

3. Dimensionless numbers

Key dimensionless parameters controlling flow and heat transfer in this study are given in Table 3.

The Prandtl number Pr is the ratio of the diffusivities of momentum and heat. For the input fluids, Pr is typically about 10, so the velocity

Table 3
Dimensionless variables

Symbol	Definition	Units	Models	Magma chamber[a]
Nu	Nusselt number	$q\Delta x/k\Delta T$		
Le	Lewis number	κ/D	150–300	10^2–10^5
Pr	Prandtl number	$\mu/\rho\kappa$	3–21 (f), 10^3 (m)	10^4–10^7
R	buoyancy ratio	$\beta\Delta C/\alpha\Delta T$	2–10	8
R_μ	viscosity ratio	μ_m/μ_f	1–225	10^2–10^4
Re	Reynolds number	$U_m\rho_m h_m/\mu_m$	10^{-3}–0.5	10^{-6}
Ra_z	Rayleigh number	$ga\rho\Delta T z^3/\mu\kappa$	10^6–10^9	10^8–10^{20}
Ra_m	melt Ra	$g(\rho_f-\rho_m)z^3/\mu_m\kappa_m$	10^6–10^7	10^9–10^{21}
St	Stefan number	$\frac{\rho_s[L_s+c_s(T_m-T_s)]}{\rho_f c_f(T_f-T_m)}$	0.6–1.8	1.1
St_m	melt St	$\frac{\rho_s[L_s+c_s(T_m-T_s)]}{\rho_m c_m(T_f-T_m)}$		
St*	St with crystallisation	$\frac{\rho_s[L_s+c_s(T_m-T_s)]}{\rho_f[f\,dL/dx+c_f(T_f-T_m)]}$	0.5–2.5	0.5

[a] Nilson et al., 1985; Huppert and Sparks, 1988; Kerr, 1994.

boundary layer is thicker than the thermal boundary layer (by a factor of $Pr^{1/2}$). The Lewis number *Le* describes the relative diffusivity of heat and compositional changes. The Reynolds number *Re* compares momentum and drag. High-*Re* flows ($Re \gg 1$) tend to be turbulent. The Rayleigh number *Ra* compares the thermal buoyancy forces, which promote convection, with the influences of viscosity and diffusion, which retard it. The buoyancy ratio *R* compares the positive compositional melt buoyancy to the negative thermal buoyancy in the boundary layers. The viscosity ratio R_μ between the melt and the input fluid affected heat transfer (thus melt rate) in the boundary layers. For icy solids, R_μ was ~ 1, whereas the wax melt was about two orders of magnitude more viscous than the fluid.

The Stefan number *St* is the ratio of the heat required to melt a solid, to the heat available to cause melting. In these experiments, *St* is the ratio of the volume of hot fluid to the maximum volume of melt produced (assuming no heat loss from the system). *St* depended principally on the latent heat L_s of the solid and the superheat $\Delta T_f = T_f - T_m$ of the input fluid relative to the melting temperature of the solid. L_s for the wax was half that of the ices (Table 2a,b), so for experiments with the same ΔT_f (all else being equal) twice the volume of wax as ice would melt. The melt rate depends on geometry and dynamics, but all other things being equal, lower *St* implies higher melt rates.

The dimensionless parameters for these models are similar to those of previous analogue experimental models (McBirney and Baker, 1985; Huppert and Sparks, 1988; Kerr, 1994), since the models are of similar scale and used similar materials. The parameters are compared with those

Table 4
Summary of experiments

Name[a]	C_f[b]	T_f	ΔT_f	ρ_f	T_{sat}	ΔT_{sat}	ΔT_s	t_{fin}[c]	Pr_f	Ra_H[d]	R_0	$R_{\mu 0}$	St_0
2WR													
P3	42	67.5–30	48.5–11	1301–1330	−1	69–31	7	20	5–11	3E8–6E6	4.5	180	1.05
P8	39.5	62–30	43–11	1281–1306	−13	75–43	8	20	5–9	3E8–5E6	4.6	180	1.20
P10	42	60–23	41–4	1307–1335	−1	61–24	4	60	6–13	2E8–1E6	5.5	150	1.18
F6[e]	24.6–22.5	30–8	32–10	1263–1250	(25–19)[f]	5-(−11)	2	30	5.5–10	2E8–2E6	5.7	2.2	2.52
F9[e]	22.3–20.3	35–13	37–15	1231–1220	(18–13)[f]	17–0	4	20	5–9	3E8–7E6	3.7	2.5	2.22
N7	38.5	45–3	47–5	1285–1315	−17.5	63–20	2	30	7–21	2E8–1E6	6.1	2	1.75
N11[e]	63.5–47	100–20	102–22	1515–1387	99–20	1–0	4	30	11–17	3E8–9E6	5.3	1.1	0.60
WR													
P13[e]	63–53	95–50	76–31	1510–1460	95–50	0	4	28	11–10	2E8–2E7	6.1	180	0.47
P14	45.3	99–45	80–26	1308–1352	13	86–32	4	25	4–9	6E8–2E7	2.8	225	0.62
N15	39	100–32	102–34	1246–1299	−16	116–48	5	13	3–9	1E9–2E7	2.2	4.3	0.85
N16	39	60–11	62–13	1278–1314	−16	76–27	5	40	5–16	4E8–4E6	4.4	2.6	1.36
N18[e]	55–45	60–12	62–14	1446–1374	58–12	2–0	4	50	11	2E8–4E6	7.4	1.2	1.23
R													
P17[e]	62.75–54	100–53	81–1	1506–1424	95–53	5–0	4	57	10–12	3E8–8E7	5.6	82	0.45
P19[e]	55–50	60–34	41–15	1446–1411	58–34	2–0	4	70	11	1.3E8–4E7	9.8	82	0.94
P20	47	100–54	81–35	1325–1363	21	79–33	4	28	4–8	6E8–1E8	3.2	200	0.61
N12[e]	62.75–47.5	100–20	102–22	1506–1395	95–20	5–0	4	180	10–17	3E8–2E7	4.6	1.1	0.64

Units: concentration *C* in wt%, temperatures *T*, ΔT in °C, density in kg/m^3, time *t* in min. $\Delta T_f = T_f - T_m$; $\Delta T_{sat} = T_f - T_{sat}$; $\Delta T_s = T_m - T_s$.

[a] First letter of experiment name indicates analogue crust: *P* = PEG-600 wax; F = $FeSO_4$–H_2O ice; N = Na_2CO_3–H_2O ice.

[b] Input fluids were solutions of $FeSO_4$ for Fn, and $NaNO_3$ for Pn and Nn.

[c] t_{fin} is the time at the end of the experiment, when the second number in a range of values applies. It might be when the model crust was melted back to the heat exchanger, or when measurements were terminated.

[d] 3E8 means 3×10^8.

[e] Means the input fluid crystallised.

[f] Non-equilibrium saturation temperature.

for a basaltic magma chamber of height 100–1000 m in Table 3. Although there are differences of orders of magnitude in some values, key parameters *Ra*, *St* and *R* overlap and others are either 'large' (*Le*, *Pr*, Ra_m) or 'small' (*Re*), so that qualitatively similar behaviour is expected. For example, the low *Re* (<1) boundary layers in the experiments and magma chambers imply laminar flow.

Additional dimensionless parameters associated with crystallisation of the input fluid are likely to be dynamically important but have not been identified in this preliminary study, thus quantitative comparisons with magma chambers are not yet possible. Crystallisation affected heat transfer and mixing and allowed compositional evolution of the input fluid.

4. Results for 2WR experiments

As listed in Table 4, seven experiments were carried out in the 2WR arrangement (Fig. 1): three using PEG wax as the solid (P3, P8 and P10), two using $FeSO_4$–H_2O ice (F6 and F9), and two using Na_2CO_3–H_2O ice (N7 and N11). Results of these experiments, including degree of wall melting, profiles of temperature and composition in the cavity, and photographs, are displayed in Figs. 3–13. The geometry and dimensionless numbers *Ra*, *Pr* and *R* were similar in these experiments. Differences arose due to variations in *St*, R_μ and whether the input fluid crystallised. As sketched in Fig. 2, common features of these experiments were: the walls melted rapidly and the roof melted very little if at all; buoyant melt flowed up the walls and collected in a layer under the roof; crystals formed in the fluid very close to the melting walls; and unless crystals

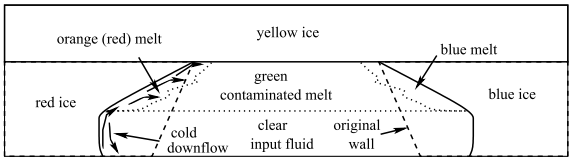

Fig. 2. Sketch of the evolution of experiment 2WR-N7. Dyed melt from the walls fed out at various levels into the contaminated melt layer at the top of the cavity. See text.

grew on the floor, a stable thermal stratification formed in the input fluid. These features are related to the nature of the boundary layers on the walls.

In Sections 4 and 4.2, the boundary layer structure and general evolution of the experiments is discussed with reference to three representative experiments, and in the succeeding Sections 4.3–4.5 particular features of individual experiments are described.

4.1. Boundary layer structure and cavity stratification

A boundary layer is a thin region between two materials (in this case the solid and the input) where material properties change rapidly. The *thermal* boundary layer is the region where the temperature changes rapidly next to the wall. Heat must conduct through this boundary layer in order to cause melting. The inner part of the thermal boundary layer is embedded in the *melt* boundary layer, where melt flows upward adjacent to the wall, while the outer thermal boundary layer extends into the input fluid. Cold fluid in the outer thermal boundary layer will tend to flow downward (Fig. 2). Nilson et al. (1985) mathematically describe counter-flowing boundary layers on a side wall.

The thermal and compositional stratifications which developed within the cavity (e.g. Fig. 3) reflect the thermal and compositional structure of the side boundary layers. The stratifications built up by the 'laminar filling box' mechanism (Worster and Leitch, 1985), in which fluid of a given buoyancy in the boundary layer feeds into the environment at its level of neutral buoyancy. After an initial stratification is set up, different parts of the boundary layer fed out at different levels depending on their densities (Fig. 2). The parts of the melt boundary layer closest to the wall were most compositionally light, so they fed to the top of the cavity. Meanwhile, the downflowing outer thermal boundary layer generated a stable thermal stratification at the bottom of the cavity. Allowing for mixing and diffusion during or after the expulsion of the boundary layer fluid, the variation of density in the environment with

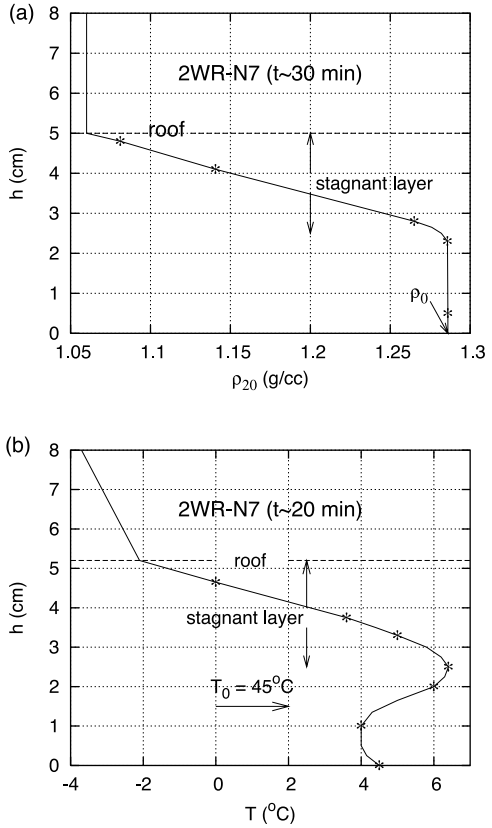

Fig. 3. Vertical profiles through the middle of the tank of (a) compositional density and (b) temperature at the times indicated for experiment 2WR-N7. Actual data points are indicated by *. The solid lines are the author's hand-drawn best guess of the continuous profiles. The 'compositional density' ρ_{20} is the density of sample as measured by the densimeter at 20°C and so does not take temperature effects into account. ρ_0 and T_0 are the initial properties of the input fluid. The arrow underneath T_0 emphasises that it is outside the range of the temperature scale of the figure.

distance from the top or bottom of the cavity reflects the systematic variation of the density of boundary layer fluid with distance from the wall (e.g. Leitch, 1987). (Note that the distance between two density levels in the environment depends on the volume flux of the intermediate densities in the boundary layer, not their distances from the wall.)

Estimates of the boundary layer thicknesses for experiments N7 and P8 are found in Appendix A. Thermal boundary layers in both experiments were about 1–2 mm thick, with thicker values applying for smaller superheats (later times). The melt boundary layers in contrast became thinner with smaller superheat. For experiment N7 the melt boundary layer was one or two orders of magnitude thinner than the thermal boundary layer (~0.1 mm). For experiment P8, on the other hand, the melt boundary layer was of comparable thickness to the thermal boundary layer at high superheat (early time) and became an order of magnitude thinner at low superheat (Fig. 24).

4.1.1. Experiment N7 – Na_2CO_3–H_2O ice

For experiment N7 the melt boundary layer generated a stable compositional stratification – the region between 2.5 and 5 cm in Fig. 3a. There was chemical diffusion through the very thin melt boundary layer as it rose (Appendix C) and the collected melt had a smooth gradient of compositions rather than a uniform eutectic composition. Because the inner thermal boundary layer was embedded in the melt layer, an associated unstable thermal stratification developed at the top of the cavity (between 2.5 and 5 cm in Fig. 3b). Since compositional effects dominated (the unstable thermal buoyancy was less than 2% of the stable compositional buoyancy) no double-diffusive layers formed.

The presence of this thick, cold, almost static layer of fluid at the top of the cavity prevented the roof from melting. Heat from the input fluid could only reach the roof by the slow process of conduction. In contrast, the walls beneath this stable layer were always in direct contact with the fluid through the thin boundary layer of melt, and they melted back rapidly.

The maximum temperature in the cavity occurred just underneath the melt layer at a height of about 2.5 cm, and below this there was a stable thermal stratification (Fig. 3b), which was set up by the downflowing outer thermal boundary layer. (The temperature inversion at the very bottom is probably due to heat released from the perspex floor.)

4.1.2. Experiments P8 and P3 – PEG-600 wax

Fig. 4 shows compositional and thermal profiles in the cavity for similar wax experiments P8

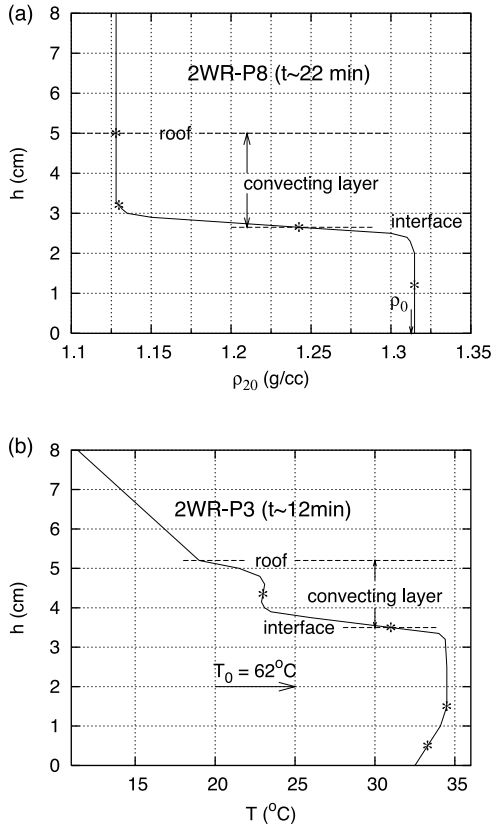

Fig. 4. (a) Profile of compositional density for experiment 2WR-P8 and (b) temperature profile for similar experiment 2WR-P3 at the times indicated. The dashed line 'interface' indicates the position of sharp density change as indicated from visual observations. See caption for Fig. 3.

and P3. In contrast with Fig. 3, the melt layer, between the roof and the interface at $h \sim 3$ cm, shows very little compositional stratification and the interface between the melt layer and the underlying fluid is very sharp. This reflects the structure of the melt boundary layer, which was relatively thick (0.5 mm compared with 0.1 mm for N7), and contaminated only at its outer edge.

For the melt layer, $Ra = g\alpha\rho\Delta T H_m^3/\mu\kappa = 8\times10^8(\Delta T H_m^3)$, which for $H_m \sim 2$ cm and $\Delta T \sim 10$°C is about 5×10^4. This is an order of magnitude higher than the critical Ra for a horizontal layer, so we expect the layer to convect thermally and produce the thermal profile sketched in Fig. 4b. The thermal stratification below the melt layer was much less pronounced than in N7 (Fig. 3b) because it was set up by a weaker outer thermal boundary layer.

Fig. 5 (plate I) is a shadowgraph photograph of experiment P3. Dark lines in a shadowgraph indicate sharp changes in refractive index, associated with changes in density and/or composition. The thick horizontal band shows the sharp interface between melt layer and input fluid, and fine striations within the melt layer outline a cellular convection pattern. Dyed melt from the opposing walls maintains separate cells, with mixing only in the middle of the layer.

The fine dark lines within the cells are too thin and sharp to be due to thermal changes. PEG wax is hydroscopic, and the absorption of water (faster than the solute ions) across the bottom of the layer would explain the thin rising sheets at the edges of the convection cells. Convection is thus driven by both thermal and compositional effects. The slight increase in compositional density of the input fluid seen in Fig. 4a may be due to the absorption of water by the wax.

4.1.3. Experiment F9 – $FeSO_4$–H_2O ice – crystallisation in the boundary layer

Experiment F9 was similar in many ways to experiment N7, but melting and cooling rates were substantially lower (Section 4.2). This is best accounted for by differences in the side boundary layer structure due to the nucleation of tiny $FeSO_4{\cdot}7H_2O$ crystals. These crystals formed a dark cloud, in which individual crystals were too small to be distinguished by eye, and they settled out near the base of the wall (Fig. 6). There was some in situ growth of slightly larger crystals ($\sim$0.5 mm) by the end of the experiment.

Compare profiles for F9 (Fig. 7) with those for N7 (Fig. 3). The temperature below the melt layer was much higher for F9, although the initial superheat was lower (Table 4 and Fig. 2b), thus cooling of the input fluid by the outer thermal flow was much less efficient. The unstable temperature gradient below the roof in F9 is also much deeper (nearly 4 cm compared with 2.5 cm for N7) and has a more complex shape. Figs. 7a and 3a confirm that there was a deeper compositional stratification for F9, with a wide weak low-

PLATE I

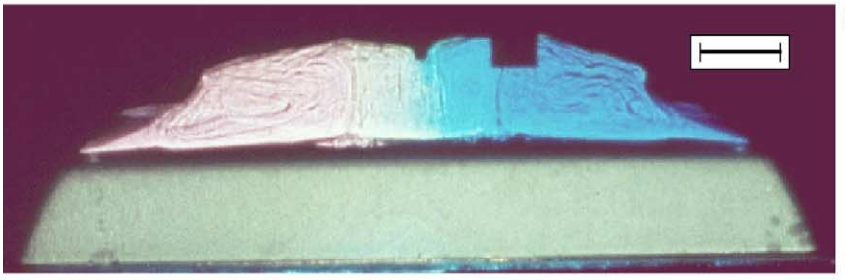

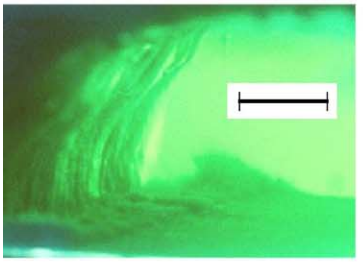

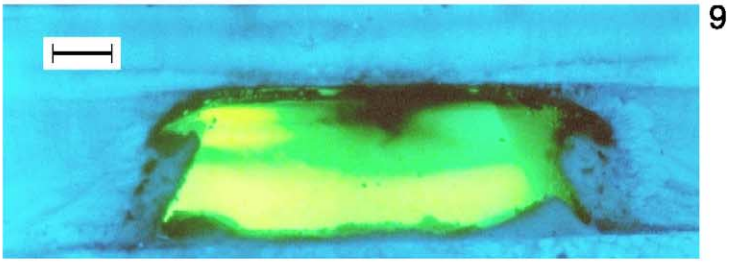

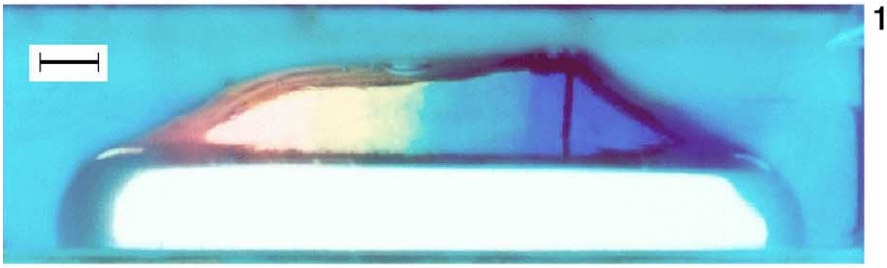

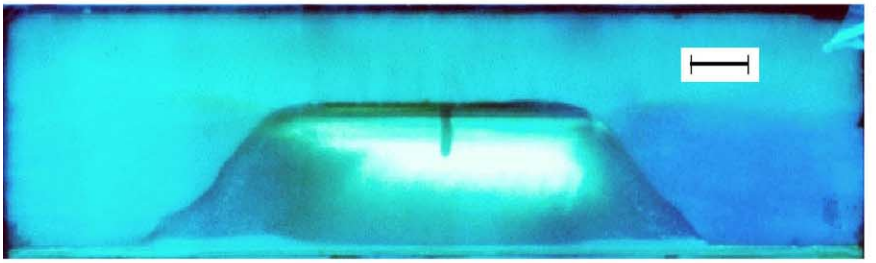

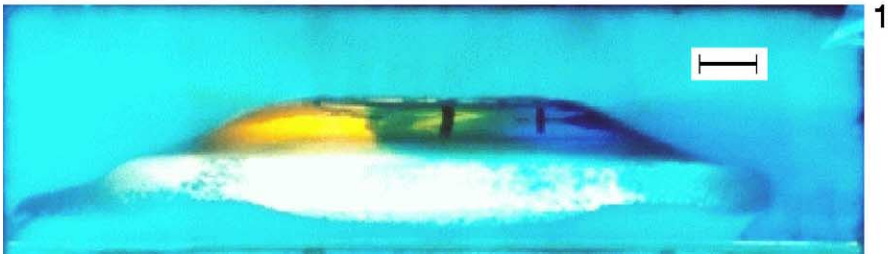

er half. (The destabilising temperature gradient in the melt layer was 7.5–16% of the compositional density gradient, insufficient to generate double-diffusive layers.)

Evidently, the compositional (melt) boundary layer for F9 was much wider than for N7. Sinking crystals of $FeSO_4 \cdot 7H_2O$ would create a counter-flow on the outer edge of the melt boundary layer, leading to strong shear and fine-scale mixing-out of the melt fluid. They would also release a light residual fluid indistinguishable from contaminated melt fluid. A rough estimate of the quantity of crystals in Fig. 6 suggests that residual fluid might account for about half of the depleted fluid in the bottom 2 cm of the compositional stratification. The wider upflowing boundary layer insulated the melting wall from the heat of the input fluid, resulting in the low melt rates observed in Fig. 8a.

4.2. Evolution of X and ΔT_f

Fig. 8 illustrates the distance the wall had melted back (X) and the superheat in the input fluid (ΔT_f) as a function of time t for three representative experiments, N7, P8 and F9. X was measured about 2–2.5 cm above the bottom of the tank, about half-way up the wall. ΔT_f was measured about midway in the input fluid below the interface. Over a timescale of 30 min, $\Delta T_f \rightarrow 0$ and X approached a limit.

A theoretical limit X_∞ can be calculated based on St, geometry and the degree of mixing, and assuming no heat gain from the environment, as described in Appendix B. Values for X_∞ are shown as arrows on the right-hand axis of Fig. 8a. The predictions are in reasonable agreement with the observations, given that there was substantial heat gain from the environment (about 10–30% of the total heat transfer at the melting walls, mainly stored heat from the plexiglass walls and floor). X_∞ was higher for F9 than for N7 because the amount of input fluid was higher (the walls were thinner and the cavity wider by 36%); however, the observed amount of melting was less, as discussed in Section 4.1.3.

The melting rate dX/dt and the superheat ΔT_f are linked, since melting is caused by superheat and superheat is absorbed by melting. Melting and cooling rates depend on the dynamics of the boundary layer. Two simple end-member models are described in Appendix C, and the results of these models are compared with experiments N7

Fig. 5. Shadowgraph photograph from experiment 2WR-P3. Note the strong interface between the melt and input fluid, and the pattern of convection shown by faint striations within the dyed melt. Time $t = 18$ min. Scale bar is 2 cm long.

Fig. 6. Closeup photograph of side wall at end stages of experiment 2WR-F9. Note the striated appearance of the wall (Na_2CO_3–H_2O ice had a similarly textured surface) and the layer of crystals on the floor at the base of the wall. The deep green colour of the $FeSO_4$ solution made dyes difficult to detect. $t = 45$ min, scale bar is 2 cm. (For interpretation of the references to colour in this figure legend, the reader is referred to the web version of this article.)

Fig. 9. Experiment 2WR-F6, where ice has melted from the cavity walls leaving a porous, refractory framework of $FeSO_4 \cdot 7H_2O$ crystals. The dark patch in the upper central cavity shows where the dyes from the melted walls, individually hard to see, have mingled. Because the input solution was more saturated than in 2WR-F9, more crystals formed (cf. Fig. 8). $t = 32$ min, scale = 2 cm.

Fig. 10. Front- and back-lit photograph of experiment 2WR-P10 ($t = 25$ min), in which the roof had a slope of 8.5°. The yellow dye in the central convecting cells is the result of roof melting. Scale bar = 2 cm.

Fig. 11. Front- and back-lit photograph of experiment 2WR-N11 ($t = 1.2$ min) showing clouds of tiny $NaNO_3$ crystals in the hot, saturated fluid next to the cavity walls, and accumulated in an uneven white layer on the floor. A thin layer of melt lies against the roof. Scale bar is 2 cm long.

Fig. 12. Experiment 2WR-N11 ($t = 6.5$ min) showing a layer of slowly interleaving melt from the two side walls, dark clouds of tiny crystals forming and sinking from the receding walls, larger crystals descending further from the walls, and a thick pile of settled crystals. The asymmetry in the melt rate of the two walls is not explained. Possibly, though there was an attempt to make the plumbing symmetrical, the right heat exchanger was colder.

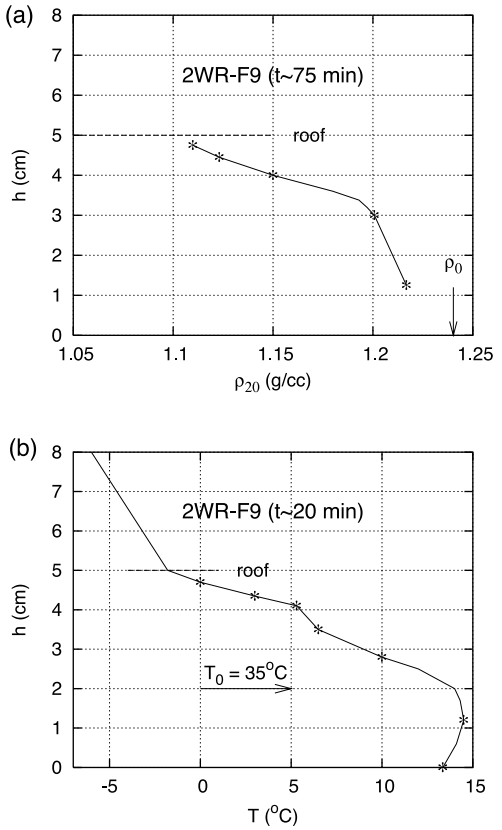

Fig. 7. Profiles of (a) compositional density and (b) temperature for experiment 2WR-F9 at indicated times. There was very little evolution of the composition from $t \approx 20$ min. The melting cavity walls evidently had a relatively enriched compositional density of about 1.1 g/cm^3 rather than the 'bulk' ρ_{20} of 1.05 g/c^3 (Section 4.3). See caption for Fig. 3.

and P8 in Fig. 8. Model 1, applied to N7, assumes that heat transfer is controlled by the downflowing thermal boundary layer, and Model 2, applied to P8, assumes that heat transfer is across an upflowing melt boundary layer. The good agreement at early time, between the models and the observations, suggests that the melting behaviour is well explained by these simple processes. The fact that Model 1 fits N7 and Model 2 fits P8 agrees well with the differing structure of the boundary layers in the two experiments, as described below. The less steeply curved shape of the lines for ΔT_f (and X) for P8 are a consequence of the weaker dependence of thermal evolution on superheat ($\Delta T_f^{3/4}$ vs $\Delta T_f^{5/4}$ see Eqs. 18 and 22). Model 1 (inappropriately) applied to P8 predicts a much faster initial melting rate.

4.3. Experiment 2WR-F6 – refractory walls

When the walls for experiment F6 were prepared (as described in Section 2) the side heat exchangers were set to −12°C and the eutectic (13 wt%) $FeSO_4$–H_2O solution froze in about a day. However, because of the nucleation barrier for $FeSO_4$ crystals, the walls near the heat exchanger were icy and the walls next to the cavity rich in interweaving refractory $FeSO_4 \cdot 7H_2O$ crystals. (To minimise this problem in experiment F9, a wall solution of 5 wt% $FeSO_4$ was used, the

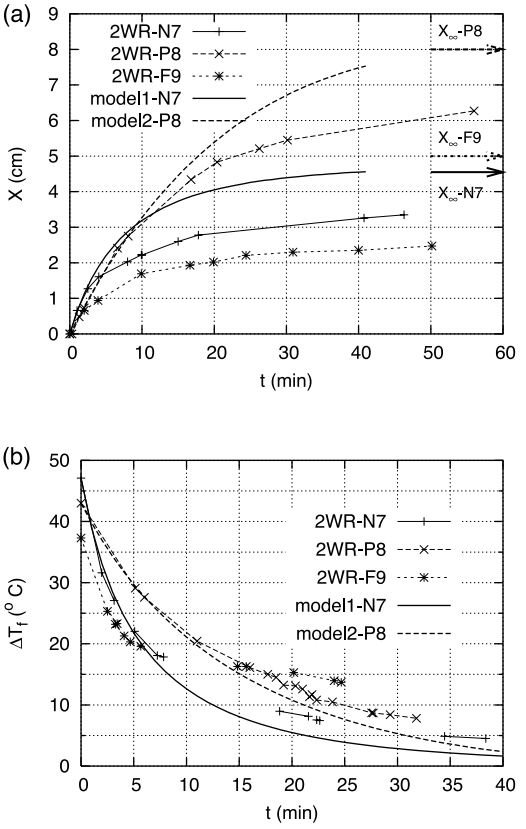

Fig. 8. Plots of (a) the amount each wall has melted back X, and (b) the superheat of the input fluid ΔT_f as functions of time for three experiments in the 2WR geometry. The dot-dashed and fine dotted lines are the predictions of models of boundary layer heat transfer presented in Appendix C. Theoretical limiting values X_∞ were calculated as set out in Appendix B.

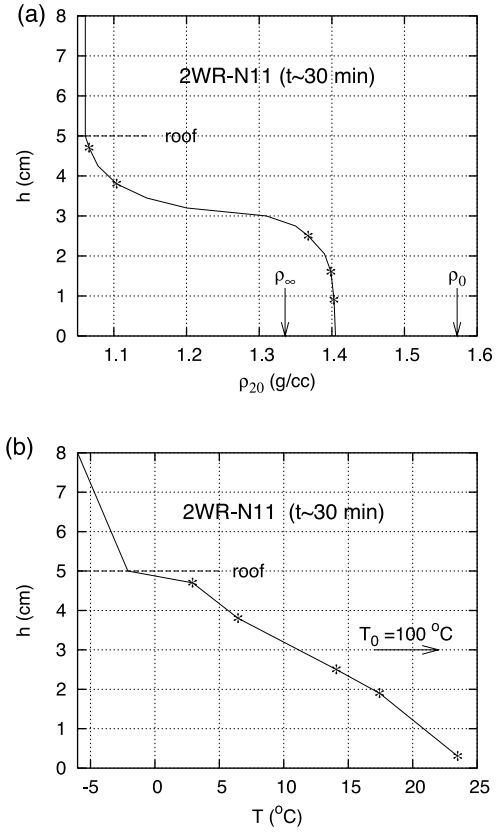

Fig. 13. Profiles of (a) compositional density and (b) temperature for experiment 2WR-N11 at $t \sim 30$ min, when melting had almost ceased. ρ_∞ is the saturation density at temperature $T_m = -2.1$°C. The higher than expected temperature at $h = 4.7$ cm probably comes about because a bubble of air lay between the roof and the fluid where the temperature profile was taken. See caption for Fig. 3.

walls were made straight, and before the experiment the most refractory bottom corners sawn off to create the usual 60° angle.)

As a consequence of their refractory composition, the walls did not melt back as they did in all other experiments. As seen in Fig. 9, pockets of ice melted from within and behind the refractory region, and watery melt from the walls collecting at the top of the cavity: despite its substantial appearance in the photograph, the refractory wall was quite porous. Meanwhile, fine $FeSO_4 \cdot 7H_2O$ crystals settled out of the thermal boundary layer. Because the walls did not move back with time, the crystals always fell in the same position and formed a steep pile. The evolution and profiles for F6 (not shown) were qualitatively similar to those of F9.

4.4. Experiment 2WR-P10 – sloping roof

In experiment P10, the roof of the cavity was higher by 1.5 cm on the right than the left. Just after the filling of the cavity, melt collected at the high end of the cavity and included yellow-dyed melt from the roof. In this early stage, the roof was effectively an extension of the sloping left wall, with a shallower angle. As in experiments P3 and P8, the melt layer broke up into squarish convecting cells with a progression of colours indicating the mixture of their sources (Fig. 10). The yellow component in the middle cells shows there is a larger contribution from the roof. Melting proceeded further on the lower end of the sloped roof (because it took longer before it was covered by the deepening melt layer), so the roof flattened.

4.5. Experiment 2WR-N11 – crystallising input

The input fluid for experiment N11 was a very hot, saturated solution of $NaNO_3$. Unlike Fe-

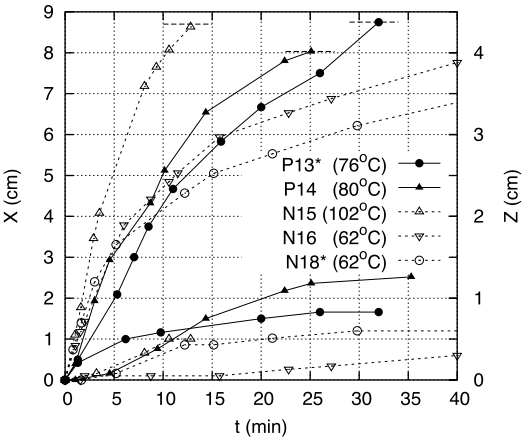

Fig. 14. Melt-back of the wall and roof with time for the WR experiments. Data for wax experiments indicated by solid symbols and unbroken lines. Circles indicate crystallisation in the input fluid. Upper curves refer to wall melting. The scale for the roof melting (right y-axis) is twice that for the wall melting. Temperatures in brackets in the key are initial superheats.

PLATE II

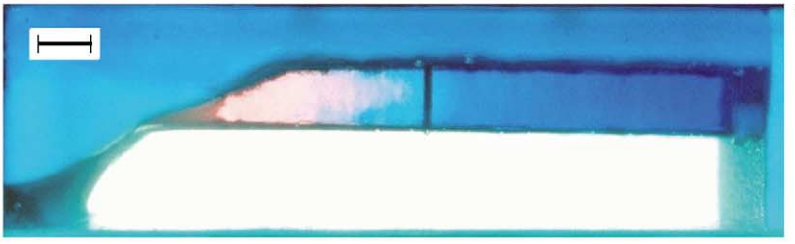
15

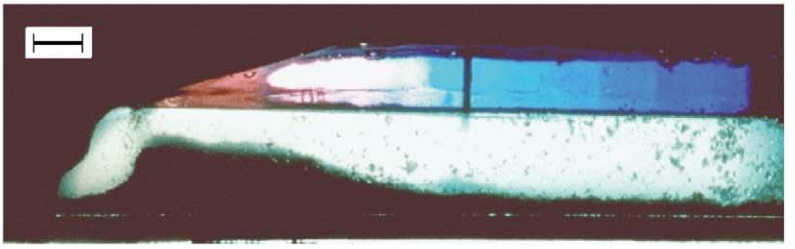
16

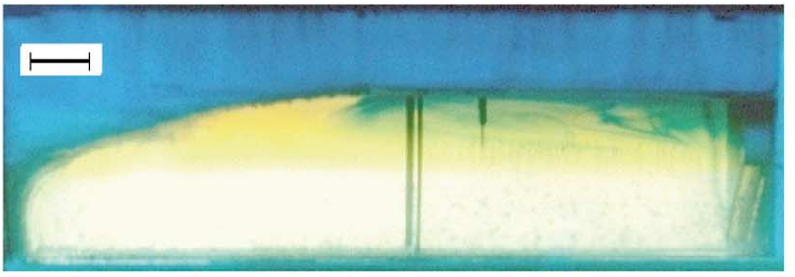
17

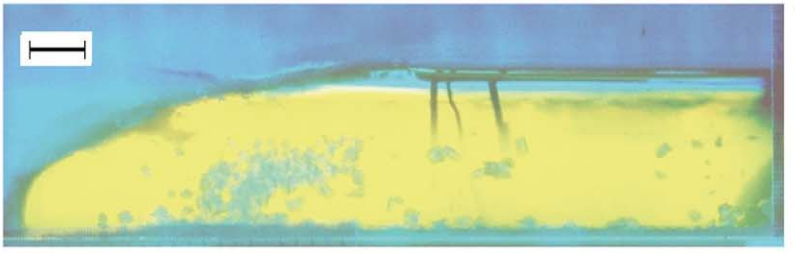
18

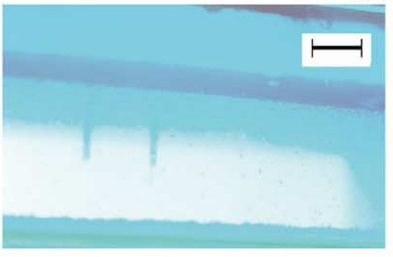
21

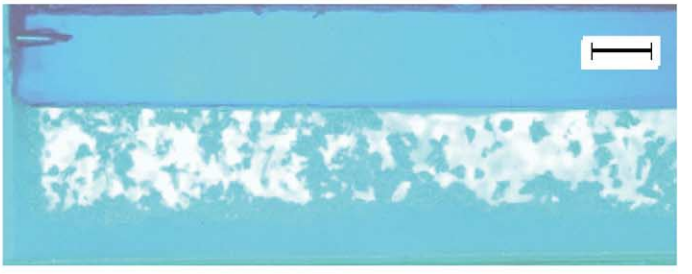
22

$SO_4 \cdot 7H_2O$ crystals, $NaNO_3$ crystals form with little supercooling. As soon as the fluid was emplaced, the entire cavity was opaque with tiny suspended crystals. Fig. 11was taken a minute after the start, when walls had already melted back 1.7 cm each. The pattern of suspended and settled crystals shows that most crystallisation took place next to the cavity walls. A rain of crystals fell from the sloping walls to carpet the floor directly underneath.

Because of the high superheat ($St = 0.62$) the experiment ran very fast: the side walls melted back dramatically while the roof did not melt. Fig. 12, taken after 6 min, shows the bottom of the left wall had melted back to the heat exchanger and melt from both walls had collected at the top of the cavity. The aspect ratio of the cavity below the melt has increased from 2.5 to 8. The coloured melt layer resembles those in Figs. 5 and 10, but rather than forming a row of convecting cells, melt in N11 flowed horizontally in from the sides. The green centre of the layer is due to light passing through a three-dimensional structure of slowing interleaving fingers of blue and yellow. Fig. 12 shows that some growing crystals were carried up by the melt boundary layer and fell when the melt joined the coloured layer. These larger crystals probably formed closer to the melt boundary layer. A hint of colour in the input fluid (bluer to the right) shows that some melt was carried down with the crystals. Note that settled crystals hindered melting of the bottom of the right wall, as predicted by Kerr (1994).

Fig. 13 displays profiles late in the evolution ($t \sim 30$ min). The temperature profile is almost linear and shows that the input fluid had lost about 85% of its superheat. The composition of the input fluid had also evolved significantly towards its asymptotic equilibrium value ρ_∞. The melt profile differs from those in N7 and F9. The faster melting rate in N11 meant the melt boundary layer was thicker, and it rose faster, allowing less time for chemical diffusion, so it was closer to a pure eutectic composition. Convection driven by the release of light residual fluid from the the in situ growth of floor crystals homogenised the fluid beneath the interface.

Although the melting rate was very high, it was

Fig. 15. Experiment WR-P14 at $t \sim 15$ min. The wax melt is coloured red from wall melting and blue from roof melting. The interface between melt and input fluid is very sharp. The wall (left) has melted unevenly, with more melting occurring at the front and back faces of the tank. Scale bar = 2 cm. (For interpretation of the references to colour in this figure legend, the reader is referred to the web version of this article.)

Fig. 16. Experiment WR-P13 at $t \sim 18$ min. The wax melt colours as for Fig. 15. The dark wavy horizontal line dissipating to the right in the melt indicates a second interface. Crystals carried up by the melt boundary layer form a thick pile with a steep scarp. There is some in situ crystallisation on the floor and front and back walls. Scale bar = 2 cm.

Fig. 17. Experiment WR-N16. Orange wall melt has collected in a stratified layer under the roof. Whisps of blue roof melt are distributed through the layer. The shadow to the left of the orange melt here and in Fig. 18 is due to a few crystals of the double salt $NaNO_3 \cdot Na_2CO_3 \cdot 10H_2O$. Scale bar = 2 cm. (For interpretation of the references to colour in this figure legend, the reader is referred to the web version of this article.)

Fig. 18. Experiment WR-N18. Stratified orange wall melt underlies blue roof melt. Large crystals of $NaNO_3$ grow on the floor and front wall. Scale bar = 2 cm. (For interpretation of the references to colour in this figure legend, the reader is referred to the web version of this article.)

Fig. 21. Experiment R-P17 at $t \sim 7.5$ min, looking upward at the wax–fluid interface. The deep blue wax melt layer is about 8 mm deep. Note that the solid–melt interface is wavy on a centimetre scale, the melt–fluid interface is covered with crystals, and that there is a layer of crystals on the bottom of the cavity. Two temperature probes pierce the roof and wax layer. Scale bar = 2 cm. (For interpretation of the references to colour in this figure legend, the reader is referred to the web version of this article.)

Fig. 22. Final state of experiment R-P17. The wax has melted completely, there is a sharp interface between wax and input fluid and a thick layer of crystals on the floor. The crystals growing on the front wall are evenly distributed with height, suggesting the input fluid was not compositionally stratified. Scale bar = 2 cm.

about a factor of two slower than predicted by Model 1 (Appendix C). The thicker melt boundary layer and the presence of crystals would have contributed to this.

5. Results for WR experiments

Five experiments were carried out in the WR arrangement: three using Na_2CO_3–H_2O ice, and two using PEG wax (Table 4). P13 and N18 involved crystallisation of the input fluid. The larger ratio of input volume to wall volume (compared with 2WR experiments) meant that the wall usually melted completely, before the input ran out of superheat. The larger ratio of roof-to-wall surface area allowed roof melting to occur. Otherwise, these experiments evolved similarly to the 2WR experiments.

5.1. Evolution of X and Z

Fig. 14 shows the melt-back of the walls (X) and the roof (Z) for the five WR experiments. The experiments with wax solid are shown with solid symbols, and for the experiments involving crystallisation the symbols are circles. The upper curves are for wall melting, the lower ones for the concurrent melting of the roof. The limit on X occurred when the wall melted back to the heat exchanger.

Differences in the melting rates of the walls can be readily explained by differences in St (ΔT_f) or the presence of crystals. N16 melts about 60% as fast as N15, and this correlates well with St (Table 4). Based on St, N18 should melt faster than N16, but it melted more slowly due to the crystallisation of the input fluid (see Section 4). Similarly, crystallising P13 melted more slowly than P14. Melt curves for wax solid were less steeply curved due to the difference in boundary layer structure (cf. Fig. 3a and Appendix C).

The roof melting curves in Fig. 14 show different behaviour to the curves for wall melting. The wax roofs melted more than the ice roofs, and crystallisation in the input fluid retarded melting of wax and enhanced melting of ice, as explained below.

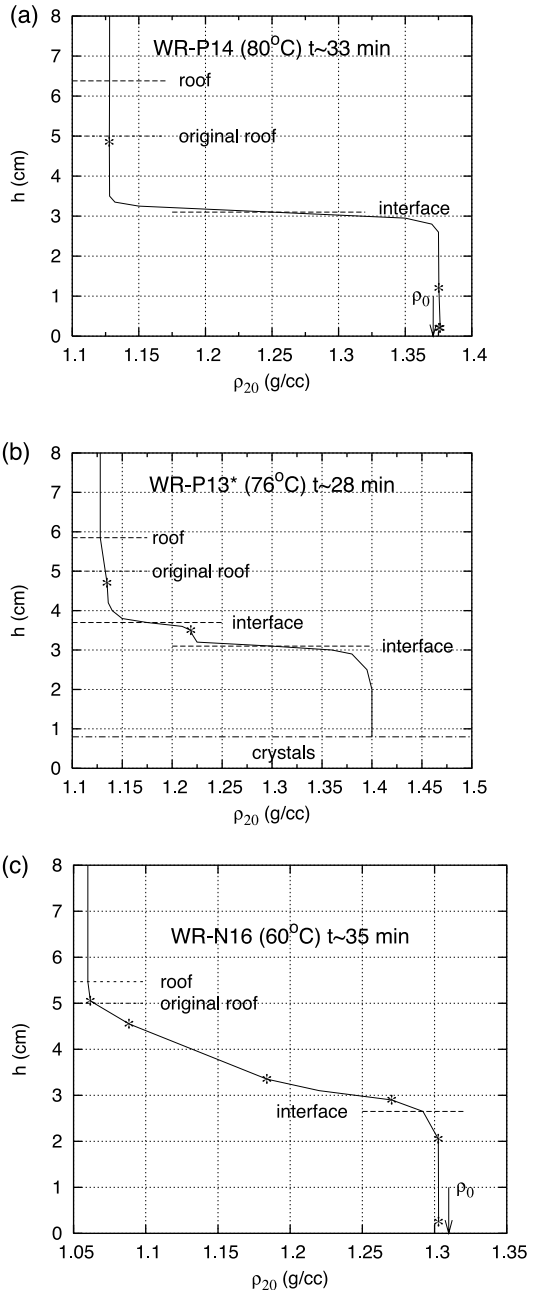

Fig. 19. Compositional density profiles for WR experiments (a) P14, (b) P13 and (c) N16. See Fig. 3 caption.

5.2. Melting and mixing of roof melts

Figs. 15–18 (plate II) are photographs from four of the experiments, illustrating the range of

behaviours seen in the systems, and Fig. 19 shows compositional density profiles for three of them.

The simplest scenario, P14, was a wax-melting experiment with high ΔT_f and no crystallisation. Fig. 15 shows that melt from the wall (pink) and the roof (blue) collected in a well-defined layer. The layer formed a series of adjacent convecting cells, with the wall melt to the left, next to the wall. The blue dye is deceptively intense: two-thirds of the melt came from the wall.

Experiment P13 was similar to P14 except that the saturated input fluid crystallised vigorously (Fig. 16). The pattern of crystallisation was similar to that in 2WR-N11, except that in P13 more of the crystals were carried up with the rising side boundary layer and dropped from the top of the melting wall, as can be seen from the steep scarp on the crystal pile. This is reasonable, since the relatively thicker melt boundary layer in P13 would have dragged upward more of the thermal boundary layer.

Particularly of note is the structure in the wax layer: instead of a single convecting layer in the vertical as in Fig. 15, there were two. The thinner lower layer was contaminated by input fluid, as demonstrated in Fig. 19b (cf. Fig. 19a). Since P13 and P14 were otherwise very similar, the crystals in P13 presumably led to disruption of the laminar melt–fluid interface, either directly as the crystals moved away from the interface, or indirectly (R.C. Kerr, personal communication) as residual liquid released from the crystals impinged on the interface. With two layers present, heat transfer from the input fluid was less efficient and hence there was less melting of the roof (Fig. 14). The initial roof melting rate is actually higher in P13 at early times. This may be due to latent heat release or enhanced convection from crystals falling from the roof, while the melt layer was still very thin.

There was little roof melting in experiment N16 because, as in experiment 2WR-N7 (Fig. 3), a thick stable compositional gradient built up under the roof, as shown in Fig. 17. The streaky horizontal pattern of blue dye shows that there was no overturning convection in the layer.

Density profiles for P14 and N16 (Fig. 19a,c) reinforce these points. Experiment P14 had a convecting layer of uniform melt composition and the roof melted significantly, whereas in N16 there was little roof melting and a broad region of stable compositional stratification. There was some exchange of water across the sharp interface in P14, indicated from shadowgraph photographs (not shown, but similar to Fig. 6) and from the slight increase in the compositional density from the initial value.

6. Results for R experiments

In the roof-only (R) experiments, the light roof melt remained in a deepening horizontal layer at the top of the cavity, a situation which was modelled experimentally and mathematically by Huppert and Sparks (1988). These authors showed that once the melt layer reached a critical thickness it would start to convect. To cause melting, heat has to be transferred from the hot fluid to the melt layer and then from the melt to the roof interface and so it is inherently less efficient than melting at a wall.

Four R experiments were carried out, one using Na_2CO_3–H_2O ice as the solid, and three using wax (Table 4). All but one (P20) involved crystallisation of the input fluid, which Huppert and Sparks (1988) discussed but did not model experimentally. The experiments show some interesting and unexpected variations in the melt rate with crystallisation and melt viscosity.

Fig. 20 shows the melt-back of the roof and the temperature evolution of the input fluid with time. Experiments P17 and P19 (solid circles and pentagons) were similar: both had saturated input fluids, though in P17 it was hotter and more concentrated. As expected, in P17 the roof melted and the input fluid cooled more rapidly – by about a factor of two, in keeping with the difference in superheat.

P20 had the same superheat as P17 but no crystallisation and, since crystallisation releases latent heat, a higher *St*. On this basis, the melt rate in P20 should be less than in P17. The significantly greater melting rate in P20 may be partly due to the lower viscosity (hence higher *Ra*) of the input fluid, and partly due to the lack of crystals. Heat

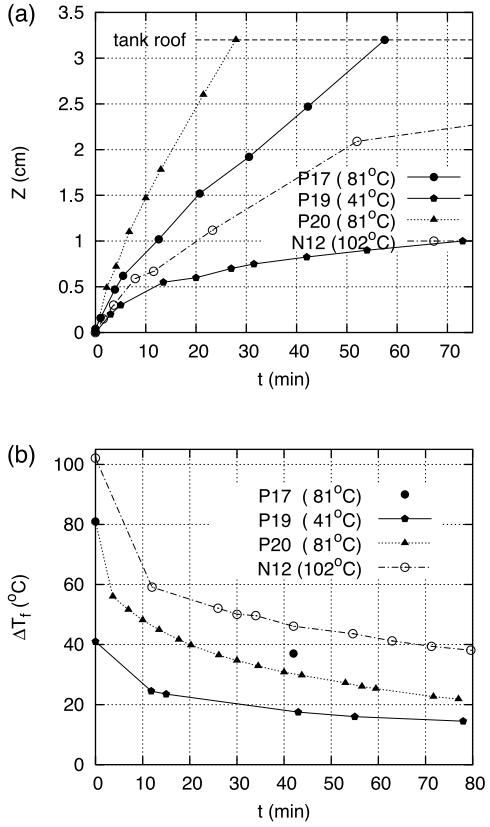

Fig. 20. (a) Melt-back of the roof and (b) superheat of input fluid with time for roof-only (R) experiments. Solid symbols and unbroken lines are for PEG-600 wax roof, open symbols for Na_2CO_3–H_2O ice roof. Rounded symbols (circles and pentagons) indicate crystallisation of the input fluid. Initial superheat given in key.

transfer across a horizontal convecting layer is proportional to $Ra^{1/3}$ (e.g. Turner, 1973), which was 45% higher for P20.

At early times in P17, crystals of $NaNO_3$ formed on the melt–input fluid interface, stuck there for some time as shown in Fig. 21 (plate II), then fell as little rafts. Crystals also grew in situ on the floor and walls of the cavity. After about 30 min only very fine crystals were stuck to the interface and falling from it. Possibly the crystals insulated the melt layer from the heat (and water?) of the input fluid, and altered the convection pattern, thus slowing the melt rate. There are no data on compositional stratification for this experiment, but Fig. 22, taken at the end of the experiment, suggests that the two layers were compositionally uniform. The input fluid would have been stirred by falling crystals, and thermal and compositional convection.

Experiments N12 and P20 had similar *St*. The melting rate depends on the heat transfer across the melt layer (about 2.4 times greater for N12 based on $Ra^{1/3}$) and the heat necessary to cause a given volume of melting (about 1.7 times greater for N12), thus the melt rate for N12 should be slightly higher than for P20 for the same superheat, and since the superheat in N12 is greater, the melt rate should be significantly higher. However, it is significantly less.

Unlike the wax-roof experiments, in N12 there was a stable compositional gradient between the roof melt layer and the input fluid, as indicated by the unstable temperature gradients in Fig. 23b. The front wall of the tank quickly became opaque with growing crystals; however, visual observation (through the crystal-free upper part of the tank wall) confirmed that there was a region 1–2 cm deep where the blue dye concentration varied from the deep blue of the pure melt to the much paler colour of the underlying fluid. The mixed region came about at least partly upon input, when the cavity was filled with clouds of tiny crystals, and it may have been enhanced by later stirring as crystals settled. Mixing between fluids is optimised when the fluids have similar viscosities: evidently this principle has important consequences even in the melting of a flat roof.

7. Summary and discussion

The present experimental study was carried out to investigate three factors which influence the interaction of mafic magma and crustal melts at the upper contacts of a magma chamber: the geometry of the contact, the viscosity contrast between melts and magma, and the crystallinity of the mafic magma. The experiments were divided into three groups, described in Sections 4–6, respectively, depending on the contact geometry. A rich variety of behaviours was observed.

For the 2WR experiments (Fig. 1 and Plate I), melting of the boundaries and thermal and com-

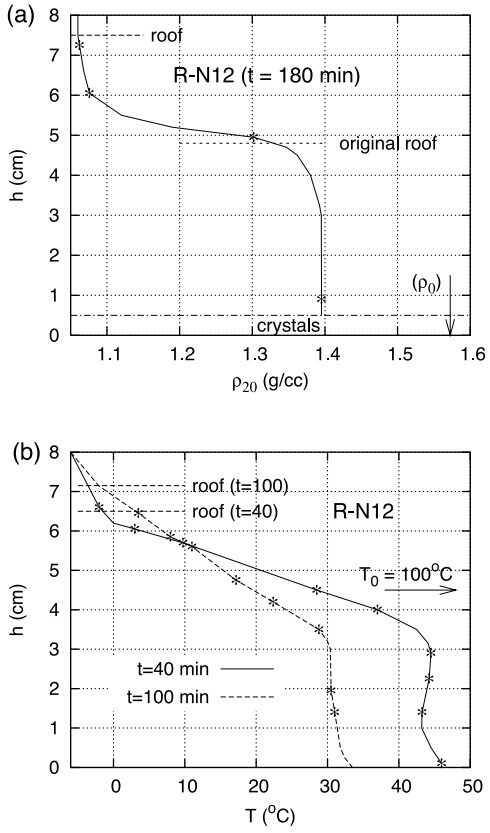

Fig. 23. Profiles of (a) compositional density and (b) temperature for experiment R-N12. ρ_0 is an extrapolation, since the fluid would be supersaturated at 20°C. See caption for Fig. 3.

positional stratification of the chamber were explained by heat and force balances in the boundary layers and the filling box mechanism (Worster and Leitch, 1985). The stratification could in fact be used to infer the structure of the boundary layer. The experiments demonstrate that side boundaries (cf. a flat roof) can dominate the evolution, because wall melting rates are much faster (Kerr, 1994) and the layer of wall melt collected at the roof can impede heat transfer to the roof. A similar result was obtained by Kaneko and Koyaguchi (2000), who showed that compositional gradients set up by simultaneous crystallisation and melting of a horizontal floor could reduce heat transfer to the roof. The WR experiments (Figs. 15–18) showed similar results except that, with a larger initial aspect ratio of the cavity, more roof melting occurred.

The viscosity contrast between melt and input fluid had a strong influence on the boundary layers and consequently the stratifications in the chamber. Inviscid melt formed a very thin boundary layer, through which chemical diffusion occurred, strongly modifying its composition (Fig. 3a). In contrast, chemical diffusion was much less significant for the thicker viscous melts, and a layer of almost pure melt built up at the top of the cavity (Fig. 4a). Uncontaminated melt formed a convecting layer (Figs. 5 and 15), whereas the stable gradient was stagnant (Fig. 17). Whether the melt accumulated at the top of the cavity was contaminated or not, mixing of the melt from the two sides of the cavity (or from the side and the roof) was a slow process, as attested by the distinct colours in the melt layers, preserved from their sources in the separate walls.

The liquidus–solidus intervals for basalts and crustal rocks are such that at a common temperature the basaltic magma will be more crystal-rich than the crustal melt (e.g. Bergantz and Dawes, 1994). The experiments with crystallisation share this property. In these experiments, there was a rapid burst of nucleation upon emplacement of the input fluid (Fig. 11), followed by continued nucleation of tiny crystals near the active melting boundary layers, principally at the side walls. Some crystals were carried up by the melt boundary layer flow before being expelled (Figs. 12 and 16), so piles of crystals accumulated at the base of the walls (Figs. 6, 9, 12 and 16). In situ growth of these accumulated crystals continued with time, and crystals also nucleated and grew on the walls and floor of the tank (Figs. 16, 18 and 22).

In almost all cases the presence of crystals slowed the melt rate. In the limit of high crystallinity, a mantle of crystals would prevent convective heat transfer to the interface. Such mantling may have played a role in the reduction of roof melting in experiment R-P17 (Fig. 21), where a thin layer of crystals was attached to the horizontal melt–fluid interface. In other experiments the slower melt rate was apparently due to: (1) a broadening of the side-wall thermal boundary layer as the crystals moved away from the interface, and (2) the related development of a broader compositional stratification under the roof (com-

pare Figs. 3 and 7). The Bagnold effect (e.g. Nilson et al., 1985), where crystals move to regions of lower shear, may have operated in the boundary layers as well as gravitational settling. The only situation where crystals enhanced melting was in the initial stages of melting the wax roof of Experiment WR-P13 (Fig. 14), perhaps due to latent heat release or the peeling away of the first-formed crystals on the roof. After that initial burst, roof melting slowed dramatically due to the insulating layer of contaminated melt that formed at the melt–fluid interface (Fig. 16). These melt-inhibiting effects were, except in experiment R-P17, associated with cross-contamination of melt and input fluid caused by physical mixing.

The effects described here rely on a dynamic melting environment, where convection allows efficient heat transfer from magma to crust, and so may be restricted to early stages after emplacement and/or a warm, hydrous crustal environment such as continental margins. Fluid movement during emplacement, which can be seen as 'forced' convection rather than the 'free' convection due to local buoyancy differences, may be important in providing such a dynamic environment. In forced convection the orientation of the contacts (roof, floor or wall) would not initially be of such importance in determining melting rates.

In both forced and free convection, an important parameter is the size of a magma injection. Relatively small injections of basaltic magma into the crust or into silicic chambers chill on both top and bottom margins and in the main retain their integrity. In contrast, Wiebe (1974, 1996) describes larger basaltic injections into silicic chambers as having bottom chills and then grading upward to a more silicic composition. Evidently there is mixing across the upper boundary of such injections, perhaps related to the mechanisms described above. Basalts rising through continental crust are inferred to be crustally contaminated (Campbell, 1985). Contamination may occur at the sides of flowing dykes or within magma chambers. In particular, very large influxes of magma associated with flood basalts may maintain the dynamic contacts where melting and contamination accompany fractional crystallisation as shown in the experiments.

Crustal rocks melt over a range of temperatures, and so there may be a tendency for a wall to disaggregate rather than melt completely. Nilson et al. (1985) argue that the position of the 'wall' may still be quite sharply defined by viscosity of the slurry. Kerr (1994) calculated melt rates for such a wall, and showed that settling velocities of individual refractory crystals within such a melt boundary layer would be negligible. However, it would be possible for clumps of crystals of several centimetres scale to sink through and lead to crustal contamination of the magma. Irregularities such as compositional banding in the crustal rocks might encourage such behaviour.

Experiment 2WR-F6 (Fig. 9) shows an interesting alternative to melt-back and/or disintegration of the walls by the input magma. With sufficient refractory material to form an interlocking framework, a low melting-point component may melt out from within the framework and rise through it. This has similarities to models of pervasive felsic magma migration proposed for other tectonic scenarios (Brown, 1994; Leitch and Weinberg, 2002). Once the low melting-point component had been extracted, the residual framework of more refractory crystals would be available for melting or partial melting by a fresh influx of hot mantle magma. Such a sequence of events is suggested by Emslie et al. (1994) to account for the variety of magmas seen in anorthosite terrains.

Processes observed in the melt boundary layers in the experiments may also occur in crystallising boundary layers, for example, nucleation within the boundary layer and broadening of the thermal boundary layer by physical mixing. Deposition of crystals from cooling boundaries has been suggested to account for sedimentary structures in mafic and silicic magma chambers (Wager and Deer, 1939; Wiebe, 1974) and continued in situ crystallisation of settled crystals is also thought to occur.

The experimental systems in this study are much simpler than geological systems, and can model only a subset of possible processes. Additional processes include: the deformation of the crust during emplacement, multiple intrusions,

venting of the magma (which probably would lead to removal of melts before a thick layer could build up), partial rather than complete melting of the crust, much more extensive crystallisation of the input magma, and late-stage melt percolation and alteration. With these provisos, the experiments help to reveal the roles that viscosity contrast and crystallinity may play in hybridisation of magmas at roof and wall contacts in magma chambers.

Acknowledgements

Funding for analysis of the experiments and production of this manuscript was provided by the author's NSERC operating grant. The experiments themselves were carried out while the author was an ARC Research Fellow at the Research School of Earth Sciences at the Australian National University. My thanks go to Tony Beasley for his excellent technical help in assisting to design and run the experiments. The manuscript benefited greatly from stimulating reviews from Ross Kerr, George Bergantz and Mark Jellinek, and helpful comments from Roberto Weinberg.

Appendix A. Properties of the side-wall boundary layers

A.1. Boundary layer thicknesses

Rough estimates of side boundary layer widths are made from simple energy balances for two representative experiments. A laminar thermal boundary layer on a flat, vertical, isothermal wall adjacent to a homogeneous environment has, for $Pr > 2$ (Worster and Leitch, 1985), a width:

$$h_T \sim \frac{2z}{Ra_z^{1/4}} \tag{1}$$

where z is distance in the direction of flow, and transition to turbulent flow starts at about $Pr\ Ra > 10^9$. (Since $Ra_z \sim z^3$, $h_T \sim z^{1/4}$.) For the experiments $Ra_z \sim 10^9$–10^6 and $Pr\ Ra \sim 1$–3×10^9 to 0.2–1×10^8 (decreasing with time) so for z of 5–3 cm, $h_T \sim 0.6$–2 mm and flow might be transitional at the beginning.

This estimate does not take into account the inner upflowing melt boundary layer. Another way of estimating h_T is from a heat balance at the interface (Kerr, 1994):

$$k_m \frac{T_f - T_m}{h_T} = [\rho_s L_s + \rho_s c_s (T_m - T_s)]v \tag{2}$$

The left-hand side is heat conducted across the boundary layer and the right-hand side is heat absorbed by the melting solid. Fig. 24 shows the measured melting rate v (unbroken line) and h_T calculated from Eq. 2 (dashed lines) for experiments 2WR-N7 and 2WR-P8. The measurement uncertainties (error bars in Fig. 24a) are large, but the results show that $h_T \sim 1$–2 mm, increasing as ΔT_f decreases. In fact, h_T is similar to predictions for a pure thermal boundary layer, 0.6–2.5 mm for 2WR-N7 and 0.75–1.3 mm for 2WR-P8.

To estimate the thickness h_m of the melt boundary layer (Kerr, 1994), we first find the melt volume flux:

$$Q \sim U_m h_m v z \tag{3}$$

where U_m is the characteristic upward velocity. Balancing the viscous and buoyancy forces in the boundary layer gives:

$$\mu_m U_m / h_m^2 \sim g(\rho_f - \rho_m) \tag{4}$$

Combining these two equations gives:

$$h_m \sim \left[\frac{\mu_m v z}{g(\rho_f - \rho_m)}\right]^{1/3} \tag{5}$$

For the ice-melting experiment 2WR-N7, the dotted line in Fig. 24a shows that $h_m \sim 0.1$ mm, an order of magnitude thinner than h_T. This increases to two orders of magnitude for small superheats ΔT_f. Basically, $h_m \sim v^{1/3}$ whereas $h_T \sim \Delta T_f / v$. Since v increases faster than linearly with ΔT_f in these experiments, h_T decreases with ΔT_f whereas h_m increases.

The significantly different scales of the boundary layers is probably the reason that calculated h_T agrees well with predictions for a flat isothermal wall. When the boundary layers have similar scales (Kerr, 1994), the melt rate decreases in the

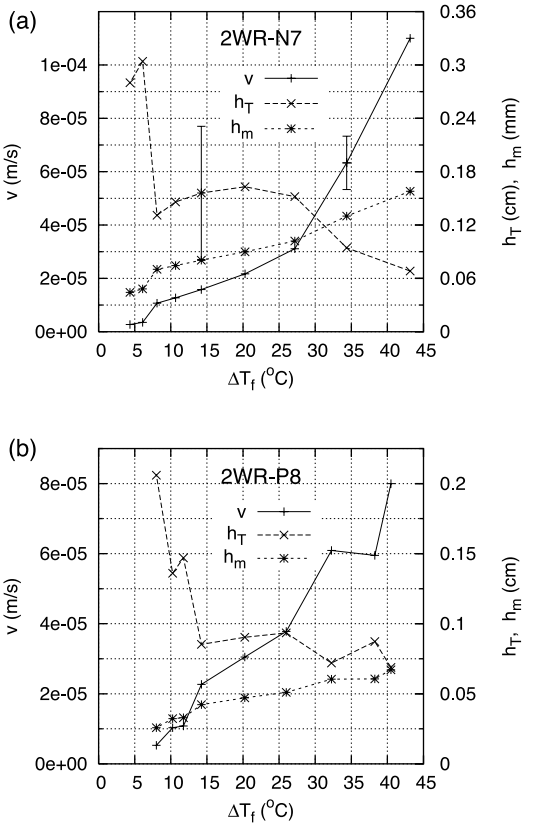

Fig. 24. Wall melt-back velocity v and boundary layer thicknesses h_m and h_T for experiments 2WR-N7 (a) and 2WR-P8 (b). Error bars indicate uncertainties. Note that the right-hand scale in panel a is in mm for h_m.

direction of melt flow (upward) because the boundary layer thickens and the thermal gradient decreases. In experiment 2WR-N7, however, the melt rate increases upward (the wall slope steepens with time) because the gradient in the downflowing thermal boundary layer increases upward, and because of the thermal stratification in the fluid (Fig. 3b).

From Eqs. 3–5 $U_m \sim 0.5$–2 cm/s for experiment 2WR-N7 and $Re = U_m \rho_m h_m / \mu_m \sim 0.5$, confirming that boundary layer flow should be laminar.

For experiment 2WR-P8 (Fig. 24) $h_m \sim 0.5$ mm, a factor of five wider than for 2WR-N7, basically because the higher-viscosity wax cannot flow up the wall as quickly as the aqueous melt. At early time $h_m \sim h_T$, so the thermal boundary layer is dragged upward by the buoyant melt (the buoyancy ratio R is 4.3–5.3) and for at least 10 min the wall slope does not steepen. After 15 min the driving temperature difference ΔT_f drops to 15°C, the boundary layer widths diverge and the melting wall quickly becomes almost vertical.

For experiment 2WR-P8, $U_m \approx 0.1$–0.5 cm/s (faster for higher ΔT_f and v) and $Re \approx 0.002$–0.02.

A.2. Boundary layer structure

In experiment 2WR-N7 melt collects in a compositionally stratified layer against the roof (Fig. 3a). There may be some physical mixing, particularly in the initial stages, but most of this stratification is likely due to chemical diffusion across the very thin melt boundary layer. For $NaNO_3$, $D \approx 8 \times 10^{-10}$ m^2/s, so in the 5 s it takes the boundary layer fluid to flow up the wall the diffusion distance is:

$$h_D \sim \sqrt{(Dt)} \sim 6 \times 10^{-5} \text{ m} = 0.06 \text{ mm} \quad (6)$$

similar to h_m.

For experiment 2WR-P8 (Fig. 5a), at the top of the cavity there is a layer of about 2 cm thick of almost pure molten wax underlain by a region of stratified fluid a few millimetres thick. It may be inferred that only the outer part of the melt boundary layer is contaminated with the $NaNO_3$ input fluid, either due to diffusion or to physical mixing promoted by countercurrent flow.

Appendix B. Maximum melt-back of walls

The maximum melt-back X_∞ of the walls can be calculated for the geometry shown in Fig. 1 assuming no heat gain from the environment, no roof melting, and that the walls beneath the melt layer are vertical most of the time (Fig. 2).

The height of the cavity is H_0 and the original widths along the bottom and top are w_b and w_t. When the walls first become vertical, the melt–input interface is at height H_1, the underlying cavity has constant width w_b and between H_1 and H_0 the width varies linearly from w_b to w_t. Then by conservation of the volume (assuming no mixing with melt):

$$H_1 = \frac{H_0}{2w_b}(w_b + w_t) \tag{7}$$

If the walls below the interface (height H) remain vertical and w is the cavity width, conservation of melt volume gives:

$$H\mathrm{d}w = -w\mathrm{d}H \tag{8}$$

$$H = \frac{H_0}{2w}(w_b + w_t) \tag{9}$$

and the amount of melt generated is given by:

$$\mathrm{d}A_m = H\mathrm{d}w \tag{10}$$

$$A_m(w) = \frac{1}{2}H_0(w_b + w_t)\left[\frac{w_b - w_t}{2w_b} + \ln\left(\frac{w}{w_b}\right)\right] \tag{11}$$

The maximum amount of melt generated by the heat available and the asymptotic width of the cavity are:

$$A_{m\infty} = \frac{H_0(w_b + w_t)}{2St} \tag{12}$$

$$w_\infty = w_b \exp\left[\frac{1}{St} - \frac{w_b - w_t}{2w_b}\right] \tag{13}$$

If a fraction f of the melt is mixed with the input fluid, such that the amount of fluid above the interface is actually $(1+f)A_m$, a similar analysis gives:

$$(1+f)A_m(w) = \frac{1}{2}H_0(w_b + w_t)\frac{2w_b(1+f)[(w_b/w)^f - 1] - f(w_b - w_t)}{f[2w_b - f(w_b - w_t)]} \tag{14}$$

$$w_\infty = w_b\left[\frac{2St\,w_b - (w_b - w_t)f^3 + (w_b + w_t)f^2 + ((2+3St)w_b - St\,w_t)f}{2(1+f)St\,w_b}\right]^{-1/f} \tag{15}$$

Appendix C. Melting and cooling rates

Approximate rates for both cooling of the input and melting of the solid can be calculated from the heat transfer at the walls. For a confined liquid of volume V, conservation of heat gives:

$$\rho_f c_f V\frac{\mathrm{d}T_f}{\mathrm{d}t} = Aq = -k_f A\frac{\Delta T_f}{H}Nu \tag{16}$$

where q is the heat flux per unit area and A is the combined area of the walls. H is the height of the walls and Nu is the dimensionless heat transfer coefficient.

C.1. Model 1 – Downflowing thermal boundary layer

If $h_m \ll h_T$, heat transfer is similar to that for a thermal boundary layer at a constant temperature wall (Appendix A and Schlichting, 1979):

$$Nu = 0.670\,Ra_H^{1/4} \tag{17}$$

For two walls Eqs. 16 and 17 give:

$$\frac{\mathrm{d}\Delta T_f}{\mathrm{d}t} = -\left[\frac{1.34}{wH^{1/4}}\left(\frac{g\alpha_f\rho_f\kappa_f^3}{\mu_f}\right)^{1/4}\right]\Delta T_f^{5/4} \tag{18}$$

where w is the width of the cavity. All variables (except g) vary with time, particularly w and H. Taking averages for w and H, Eq. 18 has the solution:

$$\Delta T_f(t) = 256\Delta T_0\,[4 + a\Delta T_0^{1/4}t]^{-4} \tag{19}$$

where the constant a (of order 10^{-3}) is the quantity in the square brackets in Eq. 18. Equating heat loss of the fluid to heat absorbed by melting gives:

$$X(t) = \frac{w}{2St_0}\frac{\Delta T_f(t)}{\Delta T_0} \tag{20}$$

where St_0 is the initial Stefan number. If allowance is made for changing w and H with time, coupled differential equations for X and ΔT_f can be solved numerically. The unbroken lines 'Model1-N7' in Fig. 8 are such numerical solutions calculated for experiment 2WR-N7. They differ little from Eqs. 19 and 20.

C.2. Model 2 – Upflowing melt boundary layer

If the thermal boundary layer is mostly embedded in the melt layer, then k_f in Eq. 16 is replaced by k_m and Kerr (1994) gives:

$$Nu = \frac{4}{3}KSt_m^{1/4}\,Ra_{mH}^{1/4} \tag{21}$$

where K is a constant ($\leq 1/\sqrt{2}$) that depends on the strength of viscous coupling between the melt boundary layer and the outer thermal boundary layer. Then Eq. 18 becomes:

$$\frac{d\Delta T_f}{dt} = -K\left[\frac{8}{3wH^{1/4}}\frac{1}{\rho_f c_f}\left(\frac{g\Delta\rho k_m^3 \rho_s (L_s + c_s\Delta T_s)}{\mu_m}\right)^{1/4}\right]\Delta T_f^{3/4} \quad (22)$$

Assuming averaged values for w and H:

$$\Delta T_f(t) = \frac{1}{256}\left[Kbt - 4\Delta T_0^{1/4}\right]^4 \quad (23)$$

where b (of order 10^{-3}) is the quantity in the square brackets in Eq. 22. $X(t)$ is given by Eq. 20. Again, numerical solutions can be found allowing for changing w and H (dashed lines in Fig. 8).

Here and in Section C.1, heat transfer varies with height along the wall – as $z^{1/4}$ in a homogeneous environment, and in a more complex way for a stratified environment – so Eq. 20 represents a vertical average. Better agreement at longer times for Model 2 and P8 (Fig. 8) may be related to the direction and smaller magnitude of the thermal stratification in the cavity (compare Figs. 3b and 4b).

References

Bergantz, G.W., 1989. Underplating and partial melting: implications for melt generation and extraction. Science 254, 1039–1095.

Bergantz, G.W., Dawes, R., 1994. Aspects of magma generation and ascent in continental lithosphere. In: Ryan, M.P. (Ed.), Magmatic Systems. Academic Press, San Diego, CA, pp. 291–317.

Bowen, N.L., 1928. The Evolution of the Igneous Rocks. Princeton University Press, Princeton, NJ, 334 pp.

Brown, M., 1994. The generation, segregation, ascent and emplacement of granite magma the migmatite-to-crustally-derived granite connection in thickened orogens. Earth-Sci. Rev. 36, 83–130.

Campbell, I.H., 1985. The difference between oceanic and continental tholeiites: a fluid dynamic explanation. Contrib. Mineral. Petrol. 91, 37–43.

Campbell, I.H., Turner, J.S., 1987. A laboratory investigation of assimilation at the top of a basaltic magma chamber. J. Geol. 95, 155–172.

CD-ROM Working Group, 2002. Structure and evolution of the lithosphere beneath the Rocky Mountains: Initial results from the CD-ROM experiment. GSA Today 12, 4–10.

DePaolo, D.J., 1981. A neodymium and strontium isotopic study of the Mesozoic calc-alkaline granitic batholiths of the Sierra Nevada and Peninsular Ranges, California. J. Geophys. Res. 86, 10470–10488.

DePaolo, D.J., Farmer, G.L., 1984. Isotopic data bearing on the origin of Mesozoic and Tertiary granitic rocks in the western United States. Philos. Trans. R. Soc. London A 310, 743–753.

Emslie, R.F., Hamilton, M.A., Theriault, R.J., 1994. Petrogenesis of a mid-Proterozoic anorthosite-mangerite-charnockite-granite (AMGC) complex: Isotopic and chemical evidence from the Nain Plutonic Suite. J. Geol. 102, 539–558.

Farnetani, C.G., Richards, M.A., Ghiorso, M.S., 1996. Petrological models of magma evolution and deep crustal structure beneath hotspots and flood basalt provinces. Earth Planet. Sci. Lett. 143, 81–94.

Frost, T.P., Mahood, G.A., 1987. Field, chemical and physical constraints on mafic-felsic interaction in the Lamarck granodiorite, Sierra Nevada, California. Geol. Soc. Am. Bull. 99, 272–291.

Hofmann, A.W., 1980. Diffusion in natural silicate melts. In: Hargraves, R.B. (Ed.), Physics of Magmatic Processes. Princeton University Press, pp. 385–418.

Huppert, H.E., Sparks, R.S.J., 1988. The generation of granitic magmas by intrusion of basalt into continental crust. J. Petrol. 29, 599–624.

Kaneko, K., Koyaguchi, T., 2000. Simultaneous crystallization and melting at both the roof and floor of crustal magma chambers: Experimental study using NH_4Cl-H_2O binary eutectic system. J. Volcanol. Geotherm. Res. 96, 161–174.

Kerr, R.C., 1994. Melting driven by vigorous compositional convection. J. Fluid Mech. 280, 255–285.

Leitch, A.M., 1987. Various aqueous solutions crystallizing from the side. In: Loper, D.E. (Ed.), Proceedings of the NATO Advanced Research Workshop on the Structure and Dynamics of Partially Solidified Systems. Martinus Nijhoff, The Hague, pp. 37–58.

Leitch, A.M., Weinberg, R.F., 2002. Modelling granite migration by mesoscale pervasive flow. Earth Planet. Sci. Lett. 200, 131–146.

McBirney, A.R., Baker, B.H., 1985. Liquid fractionation. Part I: Basic principles and experimental simulations. J. Volcanol. Geotherm. Res. 24, 1–24.

Nilson, R.H., McBirney, A.R., Baker, B.H., 1985. Liquid fractionation. Part II: Fluid dynamics and quantitative implications for magmatic systems. J. Volcanol. Geotherm. Res. 24, 25–54.

Petford, N., Cruden, A.R., McCaffrey, K.J.W., Vigneresse, J.-L., 2000. Granite magma formation, transport and emplacement in the Earth's crust. Nature 408, 669–673.

Saleeby, J., Ducea, M., Clemens-Knott, D., 2003. Production and loss of high-density batholithic root - southern Sierra Nevada, California. Tectonics (in press).

Schlichting, H., 1979. Boundary Layer Theory. McGraw-Hill, New York, 817 pp.

Thompson, A.B., Connolly, J.A.D., 1995. Melting of the continental crust: some thermal and petrological constraints on anatexis in continental collision zones and other tectonic settings. J. Geophys. Res. 100, 15556–15579.

Turner, J.S., 1973. Buoyancy Effects in Fluids. Cambridge University Press, 368 pp.

Wager, L.R., Deer, W.A., 1939. Geological investigations in East Greenland. III. The petrology of the Skaergaard intrusion, Kangerlugssuaq, East Greenland. Medd. Gronland 105, 1–346.

Washburn, E.W. (Ed.), 1926. International Critical Tables of Numerical Data: Physics, Chemistry and Technology. National Academic Press.

Wiebe, R.A., 1974. Coexisting intermediate and basic magmas, Ingonish, Cape Breton Island. J. Geol. 82, 74–87.

Wiebe, R.A., 1996. Mafic-silicic layered intrusions: the role of basaltic injections on magmatic processes and the evolution of silicic magma chambers. Trans. R. Soc. Edinb. Earth Sci. 87, 233–242.

Weinberg, R.F., 1999. Mesoscale pervasive melt migration alternative to dyking. Lithos 46, 393–410.

Weinberg, R.F., Dunlop, W.J., 2000. Growth and deformation of the Ladakh Batholith, northwest Himalayas: implications for timing of continental collision and origin of calc-alkaline batholiths. J. Geol. 108, 303–320.

Weinberg, R.F., Leitch, A.M., 1998. Mingling in mafic magma chambers replenished by light felsic inputs: fluid dynamical experiments. Earth Planet. Sci. Lett. 161, 161–177.

Weinberg, R.F., Podladchikov, Y.Y., 1994. Diapiric ascent of magmas through power law crust and mantle. J. Geophys. Res. 99, 9543–9559.

Wilson, M., Wheeler, W., 2002. Magma migration through the continental crust 3-D seismic and thermo-mechanical constraints on sites of crustal contamination. EOS Trans. AGU 83(47), Fall Meet. Suppl. Abstract V51C-13.

Worster, M.G., Leitch, A.M., 1985. Laminar free convection in confined regions. J. Fluid Mech. 156, 301–319.

Yanagi, T., Maeda, S., 1998. Magma evolution observed in the Matsuura basalts in northwest Kyushu, Japan: An example of high-pressure open system fractional crystallization in a refilled magma chamber near the crust-mantle boundary. Phys. Earth Planet. Inter. 107, 203–219.